Radio-frequency dressed lattices for ultracold alkali atoms

Article (Published Version)

Radio-frequency dressed lattices for ultracold alkali atoms

2015 New J. Phys. 17 053037

(http://iopscience.iop.org/1367-2630/17/5/053037)

IOP Publishing New J. Phys. 17 (2015) 053037 doi:10.1088/1367-2630/17/5/053037

New Journal of Physics
The open access journal at the forefront of physics

Deutsche Physikalische Gesellschaft DPG
IOP Institute of Physics

Published in partnership with: Deutsche Physikalische Gesellschaft and the Institute of Physics

OPEN ACCESS

RECEIVED
13 January 2015

REVISED
18 March 2015

ACCEPTED FOR PUBLICATION
24 April 2015

PUBLISHED
22 May 2015

PAPER

Radio-frequency dressed lattices for ultracold alkali atoms

German A Sinuco-León and Barry M Garraway

Department of Physics and Astronomy, University of Sussex, Falmer, Brighton, BN1 9QH, UK

E-mail: b.m.garraway@sussex.ac.uk

Keywords: atom chips, magnetic lattices, adiabatic dressed potentials, Bose–Hubbard model

Abstract

Ultracold atomic gases in periodic potentials are powerful platforms for exploring quantum physics in regimes dominated by many-body effects as well as for developing applications that benefit from quantum mechanical effects. Further advances face a range of challenges including the realization of potentials with lattice constants smaller than optical wavelengths as well as creating schemes for effective addressing and manipulation of single sites. In this paper we propose a dressed-based scheme for creating periodic potential landscapes for ultracold alkali atoms with the capability of overcoming such difficulties. The dressed approach has the advantage of operating in a low-frequency regime where decoherence and heating effects due to spontaneous emission do not take place. These results highlight the possibilities of atom-chip technology in the future development of quantum simulations and quantum technologies, and provide a realistic scheme for starting such an exploration.

1. Introduction

Precise control over ultracold atomic matter allows us to investigate a range of quantum phenomena with a degree of detail beyond the possibilities of standard experimental techniques used in condensed-matter and solid-state physics [1]. Through the interaction with structured static and oscillating electric and magnetic fields, it is possible to modulate most of the parameters that determine the dynamics of ultracold atomic ensembles, such as the inter-atomic potential, spin–orbit coupling and potential landscapes for the atomic centre-of-mass motion. These possibilities for control added to the capacity for real-time probing, have accredited ultracold atomic gases as powerful platforms for developing applications in quantum simulations, quantum information and quantum enhanced metrology. The study of idealized lattice models and quantum simulations has potential for uncovering the physical mechanisms behind a range of phenomena yet to be fully understood, like high temperature superconductivity [2], universality of non-equilibrium dynamics [3] and condensation in gauge theories [4].

Optical lattices, made by interfering coherent electromagnetic radiation, are common tools used to impose spatially periodic potentials over ensembles of neutral ultracold atoms [5]. An optical lattice consists of regular arrays of dipole trapping wells whose geometrical disposition and depth is controlled by the properties of the interfering radiation (polarization, intensity and frequency) and the geometry of the interference pattern. Cold atomic gases in optical lattices can form a range of discrete physical models governed by a Hubbard Hamiltonian, whose dynamics is carefully adjusted by external fields and studied via high resolution imaging of the atomic cloud. In particular, various idealized condensed matter models have been experimentally realized, exhibiting complex phenomena including metallic-to-insulating transitions [6], magnetic ordering and frustration [7] and the quantum Hall effect [8]. Importantly, in pure optical lattices, the periodicity of the resulting potential landscape is limited by diffractive effects, being of the same order of magnitude than the radiation wavelength, and corresponding to a few hundred nanometres for the case of alkali atoms. This restricts the possibility of an optical lattice having a significantly smaller spacing, or for the lattice to have a variation in trap geometries; both elements being key to observe the dynamics of quantum lattice models deeply in the regime of superexchange rate [9].

Fine control over ultracold atomic gases is also possible using atom-chip configurations, where the potential landscape for the atomic centre-of-mass motion is produced by micron-sized sources of low-frequency fields

(dc, radio-frequency and microwaves) [10]. In this context, various experiments have demonstrated trapping of neutral cold atoms in one-dimensional (1D) and two-dimensional (2D) periodic potentials, using *static* magnetic fields (dc) produced by arrays of carefully sculptured permanent magnets [11–16]. Two-dimensional arrays of magneto-optical traps mounted on the surface of atom-chips have been also demonstrated, requiring simple patterns of current carrying conductors [18, 19] or sculptured pyramidal-mirrors [20]. The lattice constant of the periodic landscapes produced by such schemes ranges from a few mm down to 10 μm, and is limited by fabrication technology and near-surface effects [10]. Recent proposals suggest that this atom-chip approach can, in principle, create arrays of magnetic traps with submicron periodicity, located a few hundred nanometers away from the chip surface [21, 22]. Experimental realization of such proposals face technical challenges associated with the complexity of their fabrication and from the short surface-atom distance which enhances near surface effects.

Atom-chip technology has greatly benefited from dressing techniques, in which the Zeeman splitting in an inhomogeneous magnetic field is modified by coupling atomic hyperfine states with a radio-frequency magnetic field (RF) [23, 24]. The resulting potential landscape depends on the vector nature of both fields (dc and RF) [25], which can be exploited to define complex potential landscapes without the limitations imposed by the Maxwell equations dominating purely magnetic traps [24]. This characteristic allows the creation of trapping configurations with non-trivial topologies, such as ring [24] and toroidal traps [26], using simple layouts of micro-fabricated conductors and magnets. In addition, atom-chip technology has been key in developing procedures for the coherent manipulation of Bose–Einstein condensates [27] with potential for creating quantum hybrid systems for a wide range of applications [28].

In this paper we describe an atom-chip setup that produces a 2D periodic potential, created by arrays of straight current-carrying conductors plus a uniform oscillating field. The periodicity and well depth of the resulting potential landscape is comparable to optical lattices (as in, e.g., [6]) and arrays of magnetic traps (as described in [29]). This suggests that atoms loaded in the RF-dressed lattice potential can easily reach the Bose–Hubbard regime, where the superfluid-to-Mott-insulator phase transition has been observed [6], and here we study the range of parameters that can be realized with currently available atom-chip technology. Importantly, the approach here described is convenient for scaling down the lattice spacing below the range accessible by optical means, which is crucial for reaching the strong coupling regime at temperatures of a few nano-kelvin [2] and paves the way to develop applications in quantum simulation, lattice clocks and quantum information, benefiting from the high mechanical stability and compact nature of the atom-chip technology.

2. Radio frequency dressed potential

Adiabatic potentials arise whenever a near-resonant or resonant field couples internal atomic states experiencing different potentials for the atomic centre-of-mass motion [23]. Here, we consider an alkali atom in its ground state moving across a region of inhomogeneous magnetic field $\boldsymbol{B}(\boldsymbol{r},\ t)$, which couples states within a single hyperfine state manifold. The atomic motion is described by the Hamiltonian

$$H = \frac{\boldsymbol{p}^2}{2m} + g_F \mu_B \boldsymbol{F}\cdot\boldsymbol{B}, \tag{1}$$

with $\boldsymbol{p}$ the atomic linear momentum, $\boldsymbol{F}$ the atomic total angular momentum and g_F the Landé gyromagnetic factor. The magnetic field has spatially varying static and oscillating components of the form

$$\boldsymbol{B} = \boldsymbol{B}_{\rm dc}(\boldsymbol{r}) + \boldsymbol{B}_{\rm RF}(\boldsymbol{r})\cos(\omega_{\rm RF} t). \tag{2}$$

After applying the rotating wave approximation (RWA) and neglecting non-adiabatic couplings [23, 24], the atomic dynamics is described by the effective Hamiltonian

$$H_{adb} = \frac{\boldsymbol{p}^2}{2m} + \sqrt{\left(\left|\mu_B g_F \boldsymbol{B}_{\rm dc}\right|^2 - \hbar\omega_{\rm RF}\right)^2 + \left(\frac{\mu_B g_F \left|\boldsymbol{B}_{\rm RF,\perp}\right|}{2}\right)^2}\, F_z, \tag{3}$$

where $\boldsymbol{B}_{\rm RF,\perp}$ is the component of the RF field orthogonal to the dc field. The second term on the right-hand side of this equation defines the dressed potential energy, $V_{adb}(\boldsymbol{r})$. The two contributions under the radical symbol have a clear physical interpretation: the first one corresponds to the detuning of the driving field with respect to the Zeeman splitting of the hyperfine states, and the second term defines the effective coupling between hyperfine states. The spatial variation of the static and dressing fields therefore translates into a modulation of the potential energy landscape experienced by the atomic centre-of-mass motion.

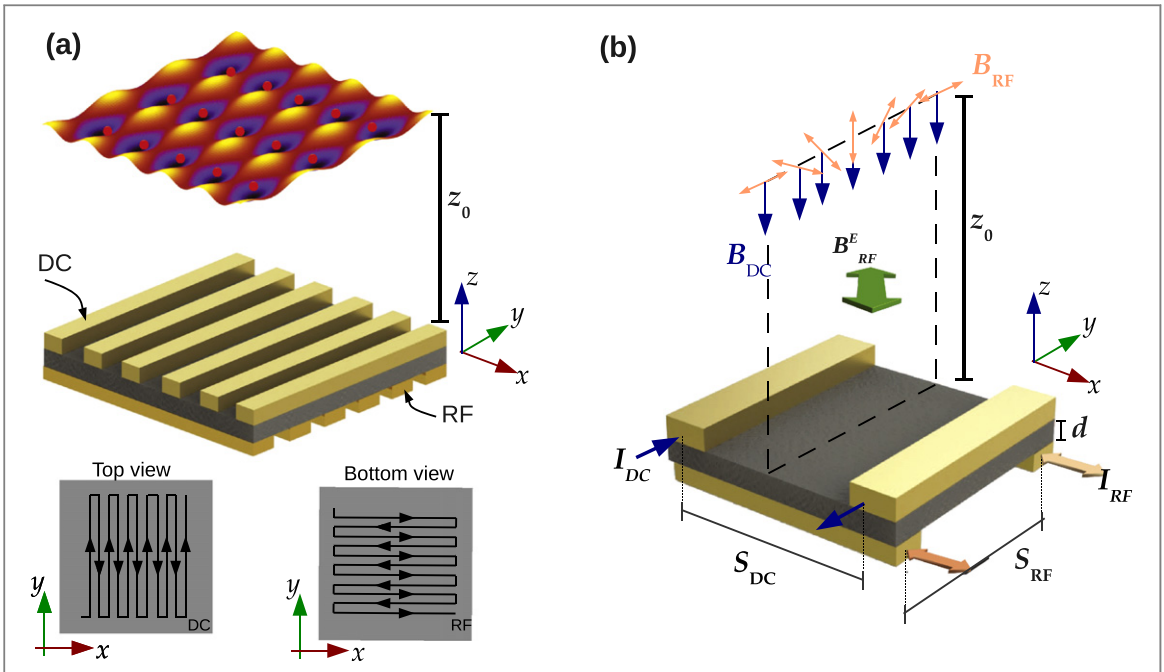

Figure 1. Atom-chip design of an RF-dressed lattice potential (a) crossed arrays of parallel conductors and schematic of the potential landscape experienced by ultracold neutral alkali atoms. The lower two panels show extended top and bottom views of the conductor arrays. (b) Close-up of the central part of a unit-cell of the conductor array seen in (a). Conductors oriented parallel to the x-axis (y-axis) carry RF (dc) currents, producing a magnetic field that dresses Zeeman split atomic states. Additional control over the potential landscape is gained through a uniform RF field (green arrow). Light (orange) and dark (blue) arrows indicate fields produced by currents with corresponding colours. Dashed lines are included to guide the eye. Notice that along the upper dashed line, the static field (dark arrows) points downwards, while the direction of the RF field (light arrows) rotates in the y–z plane. Also, above the geometrical centre of the shown conductor array the dc and RF fields are oriented along the z direction, making $B_{\mathrm{RF},\perp} = 0$ (see text).

3. Device configuration and potential landscape

We consider two crossed arrays of parallel current-carrying conductors as schematically shown in figures 1(a)–(b). Conductors aligned parallel to the y-axis carry dc currents with alternating directions between neighbouring wires of width w_{dc}. The second array, oriented parallel to the x-axis, carries RF currents with a phase difference of π between neighbouring conductors. These RF conductors have a width w_{RF}. The combination of static and RF magnetic fields, created by this current distribution, produces a periodic potential landscape with spatial periodicity equal to the centre-to-centre distance between conductors.

To gain insight into the resulting potential landscape, we initially consider the limit of single filament conductors, i.e. the width $w_{\mathrm{dc,RF}} \to 0$, and study the field distribution at large distances from the conductor array, which corresponds to take $z \gg \max\{S_{\mathrm{dc}}, S_{\mathrm{RF}}, w_{\mathrm{dc}}, w_{\mathrm{RF}}\}$ with S_{dc} and S_{RF} being the centre-to-centre distance between dc and RF conductors, respectively. Other parameters are indicated in figure 1. In this case, the fields have a simple harmonic spatial dependence given by [10]

$$\begin{aligned}\boldsymbol{B}_{\mathrm{dc}} &\approx B^0_{\mathrm{dc}} \mathrm{e}^{-k_{\mathrm{dc}} z}(-\cos(k_{\mathrm{dc}} x)\hat{\boldsymbol{x}} + \sin(k_{\mathrm{dc}} x)\hat{\boldsymbol{z}}),\\ \boldsymbol{B}_{\mathrm{RF}} &\approx B^0_{\mathrm{RF}} \mathrm{e}^{-k_{\mathrm{RF}}(z+d)}(-\cos(k_{\mathrm{RF}} y)\hat{\boldsymbol{y}} + \sin(k_{\mathrm{RF}} y)\hat{\boldsymbol{z}})\cos(\omega_{\mathrm{RF}} t),\end{aligned} \tag{4}$$

where B^0_{dc} and B^0_{RF} are the amplitudes of the fields at the surface of the conductors (i.e. $z = 0$ and $z = -d$, for the dc and RF wires in figure 1, respectively), and $k_{\mathrm{dc,RF}} = \pi/S_{\mathrm{dc,RF}}$. The dressing frequency sets a resonant plane at $z = z_0$ defined by $\hbar\omega_{\mathrm{RF}} = \mu_B g_F |B^0_{\mathrm{dc}}| \mathrm{e}^{-k_{\mathrm{dc}} z_0}$. With this field setup, the dressed potential landscape, given by (see section 2)

$$V_{adb} = \sqrt{\left(\left|\mu_B g_F \boldsymbol{B}_{\mathrm{dc}}\right|^2 - \hbar\omega_{\mathrm{RF}}\right)^2 + \left(\frac{\mu_B g_F \left|\boldsymbol{B}_{\mathrm{RF},\perp}\right|}{2}\right)^2} \tag{5}$$

consists of a regular array of 3D trapping sites centred at $\boldsymbol{r}_0 = (mS_{\mathrm{dc}}/2,\ nS_{\mathrm{RF}}/2,\ z_0)$ with $m,\ n \in \mathbb{Z}$, as shown in figures 2(a) and (b) for the state $|F = 1,\ m_F = -1\rangle$ of ^{87}Rb.

At the centre of each trapping site the dressing is resonant (i.e. the detuning is zero). In addition, the RF field oscillates along the direction of the static field, which makes the effective dressing field $|\boldsymbol{B}_{\mathrm{RF},\perp}|$ equal to zero. This configuration would then suffer from large Landau–Zener transition rates to untrapped states because of the

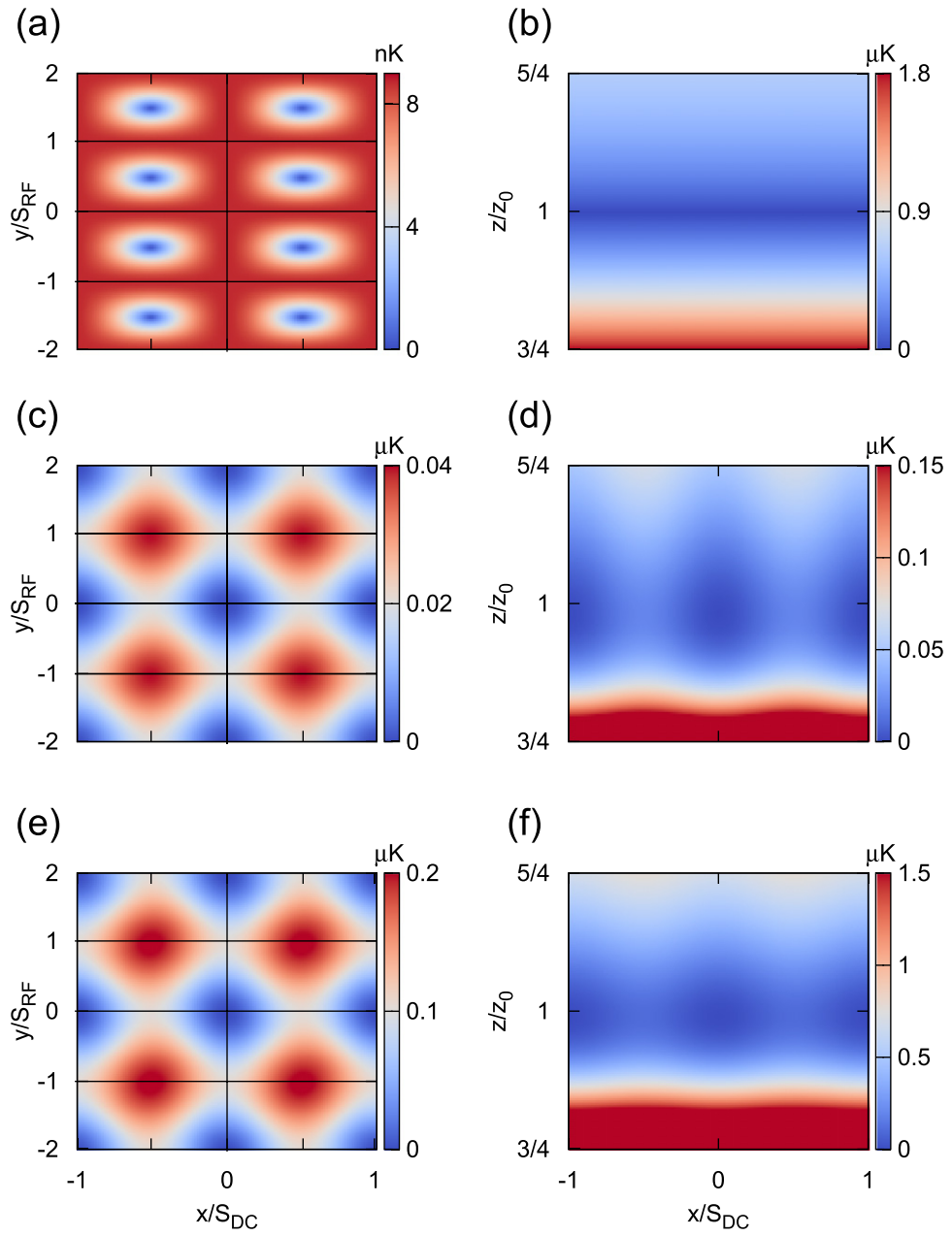

Figure 2. Periodic potential landscapes: single-filament versus finite-width conductors radio-frequency dressed lattices for the state $|F=1,\ m_F=-1\rangle$ of ^{87}Rb, at planes $z=z_{\min}$ (left column) $y=0$ (right column), as defined in figure 1. In all cases, the colorbar scales corresponds to $d=400$ nm, $S_{\rm RF}=1.0\ \mu$m, $S_{\rm dc}=1.5\ \mu$m, $z_0=2\ \mu$m, $B^0_{\rm dc}=2$ G, $B^0_{\rm RF}=1.0$ G. Other parameters: (a)–(b) $w_{\rm RF,dc}=0$ and $\boldsymbol{B}^E_{\rm RF}=\boldsymbol{0}$, (c)–(d) $w_{\rm RF,dc}=0$, $\boldsymbol{B}^E_{\rm RF}=(26.7,\ 304.5,\ 0)$ mG, $\omega_{\rm RF}/2\pi=21.2$ kHz, (e)–(f) $w_{\rm RF,dc}=0.5\ \mu$m, $\boldsymbol{B}^E_{\rm RF}=(61.4,\ 304.5,\ 0)$ mG, $\omega_{\rm RF}=84.9$ kHz. The external field, $\boldsymbol{B}^E_{\rm RF}$, is zero in panels (a) and (b), and satisfies equation (7) in panels (c)–(f). Solid black lines indicate the position of dc and RF conductors.

simultaneous vanishing of the two terms defining the dressed potential energy equation (5) [10]. However, this hole in the potential energy landscape can be closed by adding a uniform RF field that oscillates at the same frequency of the RF conductors, parametrized by

$$\boldsymbol{B}^E_{\rm RF}=B^E_{{\rm RF},x}\cos(\omega_{\rm RF}t+\psi)\hat{\boldsymbol{x}}+B^E_{{\rm RF},y}\cos(\omega_{\rm RF}t+\phi)\hat{\boldsymbol{y}}. \tag{6}$$

In general, to ensure that there are no points in the space where the effective dressing field and the detuning are both zero simultaneously, the external field should satisfy $|B^E_{{\rm RF},y}|>B^0_{\rm RF}e^{-k_{\rm RF}(z_0+d)}$ (see appendix A).

For simplicity, we initially consider a linearly polarized external field whose components oscillate in phase with the reference RF conductor, i.e. $\psi=\phi=0$ in equation (6). This external uniform field has two effects on the dressed potential produced by the array of conductors as may be seen in figures 2(c), (d). Firstly, the spatial period is doubled along the y direction (orthogonal to the RF current flow). This occurs because the RF field produced by the conductor array has opposite directions above the centre of consecutive RF conductors, (see

equation (4)) in such a way that the total RF field repeats itself every other RF wire. The periodicity of the potential along the x direction depends on the static magnetic field, and is therefore not affected by the applied field $\boldsymbol{B}^{E}_{\mathrm{RF}}$. Secondly, the minima of the potential energy equation (5) localizes above the intersections of the dc and RF conductors (e.g. $(x,\ y) = (0,\ 0)$ in figure 1(b)), at a vertical distance $z_{\mathrm{min}} < z_0$ from the chip surface. In general, the vertical position of dressed energy minima should be evaluated numerically (see appendix A). Thus, with the additional external field, the potential landscape consists of a set of trapping centres located at positions $\boldsymbol{r}_{\mathrm{min}} = (mS_{\mathrm{dc}},\ 2\ nS_{\mathrm{RF}},\ z_{\mathrm{min}})$, with $m,\ n,\ \in \mathbb{Z}$.

The energy barrier between consecutive wells can be controlled by the applied uniform field and the current through the conductors. In the limit of single filament conductors, for example, a rectangular symmetric 2D lattice, in which the barrier height of the potential along the x and y directions are the same, we require the condition

$$B^{E}_{\mathrm{RF},x} = 2\sqrt{B^{E}_{\mathrm{RF},y} B^{0}_{\mathrm{RF}} \mathrm{e}^{-k_{\mathrm{RF}}(z_{\mathrm{min}}+d)}}. \tag{7}$$

An example of the potential landscape resulting from such a field and current configuration is shown in figures 2(c) and (d), again for the state $|F = 1,\ m_F = -1\rangle$ of ^{87}Rb.

The fast decay of the field amplitude with the distance from the conductors and practical limitations over the current tolerated by micron-sized conductors, implies that strong trapping configurations are feasible at relatively close proximity of the conductor arrays. Therefore, evaluating the field distribution requires us to take into account the finite size of the conductors. Here, we evaluate numerically the field distribution and corresponding dressed energy landscape, produced by conductors with finite width and negligible height [10] (see appendix B). For comparison with the single-filament case, in figures 2(e)–(f) we present the resulting potential landscape produced by an array of conductors with dimensions $w_{\mathrm{dc}} = w_{\mathrm{RF}} = 0.5\ \mu$m, $S_{\mathrm{dc}} = 2.0\ \mu$m and $S_{\mathrm{RF}} = 1.5\ \mu$m, and fields and currents adjusted to produce a rectangular symmetric potential landscape, at a distance $z_0 = 2.0\ \mu$m from the surface of the dc conductors.

The importance of finite size effects are evident after comparing the energy scales in panels (c)–(d) with (e)–(f) of figure 2, which differ by almost one order of magnitude. Such a large difference occurs because, in the case of conductors with finite width, the decay of the amplitude of the fields with distance z from the surface is significantly slower than exponential near the surface. Thus, considering configurations with the fields of equal amplitude at the conductor surfaces, resonant dressing at a given z_0 is produced by RF-frequencies ω_{RF} significantly different from the single filament case. Similarly, given an external applied field with y component $B^{E}_{\mathrm{RF},y}$, the x component required to produce a rectangular symmetric lattice is larger in the finite width case, as indicated in the caption of figure 2.

To show the flexibility of our proposal, we determine numerically the equivalent of condition equation (7) for the case of finite conductors. We also evaluate the curvature of the potential energy at the potential minima (in units of frequency, or trap frequency ν_{trap}) and the energy barrier between consecutive wells, corresponding to a range of parameters typically accessible with atom chip configuration (e.g. [28]). We observe that the field required to produce a symmetric potential landscape can be accurately evaluated after substituting in equation (7) the factor $B^{0}_{\mathrm{RF}}\mathrm{e}^{-k_{\mathrm{RF}}(z_{\mathrm{min}}+d)}$ by the amplitude of the fields calculated numerically at the centre of any trapping site. This agreement is shown in figure 3(a).

The geometry of the lattice can be controlled via pairs of parameters defining the dc and RF fields. For example, rectangular symmetric lattices with a desired inter-well barrier can be produced either adjusting the two components of the external field, $\boldsymbol{B}^{E}_{\mathrm{RF}}$, or one of its components and the inhomogeneous RF field through B^{0}_{RF}. This last case is shown in figure 3(c).

3.1. Other lattice geometries

The regular lattice shown previously is one of many possibilities we have at reach by adjusting the fields and currents in the device. In particular, the symmetric potential in figure 2 can be deformed into an array of 1D chains parallel to the array of conductors, simply by using an external field that does not meet the condition equation (7). This is shown in figure 4(a), where an applied field smaller than required by equation (7) produces an array of chains oriented parallel to the RF conductors (x direction). In its turn, an applied field larger than this condition produces an array of 1D chains oriented along the RF conductors (y direction), as in figure 4(b). Notice that a smooth transformation of the potential landscape between such configurations is possible following a slow variation of the currents and applied field.

The phase of both components of the uniform applied field with respect to the currents in the conductors provides an additional degree of freedom, which can be employed to define lattices with geometries of interest for quantum simulation [30]. Following the RWA and in the frame of the local static field, the effective dressing fields are given by

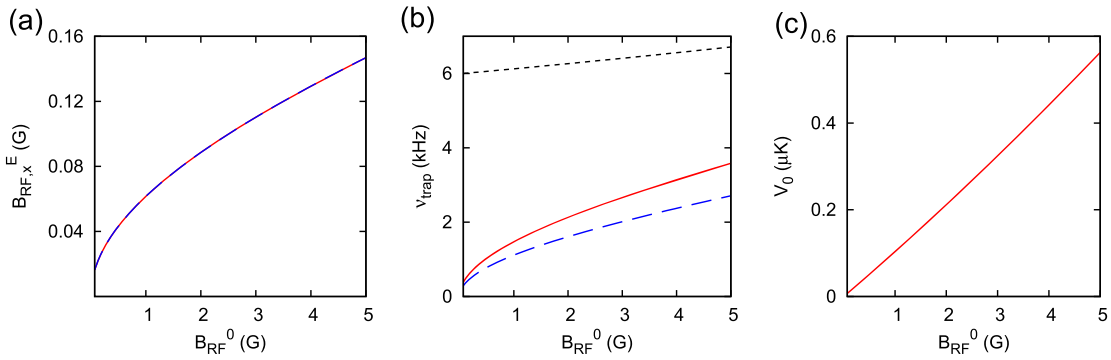

Figure 3. Properties of a rectangular symmetric lattice as function of dressing field $B^0_{\rm RF}$, for the state $|F=1,\ m_F=-1\rangle$ of ^{87}Rb. (a) Component of the external field $B^E_{{\rm RF},x}$ required to produce a rectangular symmetric potential lattice: numerically evaluated (solid) and determined by equation (7) using the numerical value for $B_{\rm RF}(z_{\rm min})$ (dashed). (b) Local frequencies at the minimum of the potential landscape: $\nu_{\rm trap}$ is $\omega_z/2\pi$ (short-dashed), $\omega_x/2\pi$ (solid), $\omega_y/2\pi$ (dashed). (c) Inter-well barrier V_0. For all panels $w_{\rm dc}=w_{\rm RF}=0.5\ \mu$m, $S_{\rm RF}=1.0\ \mu$m $S_{\rm dc}=1.5\ \mu$m, $z_0=2.0\ \mu$m, $\omega_{\rm RF}=84.9$ kHz, $B^0_{\rm dc}=2.0$ G, and $B^E_{{\rm RF},y}=0.3$ G.

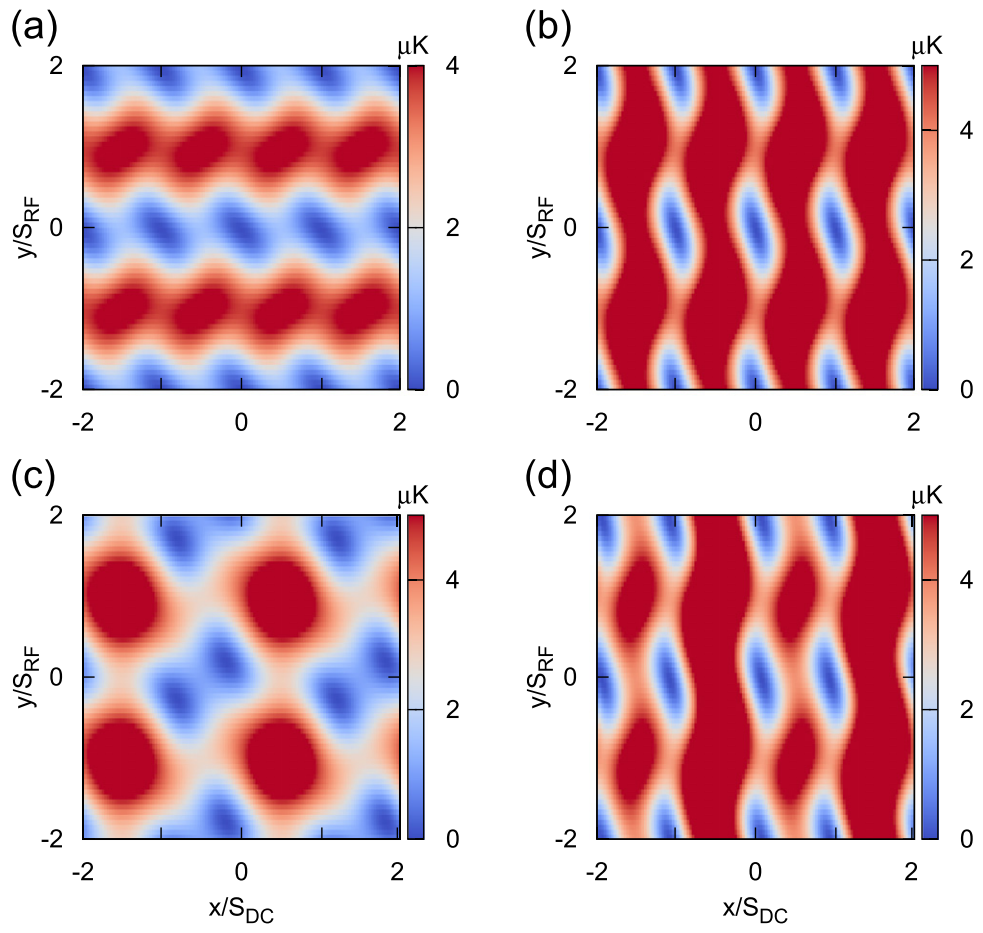

Figure 4. Lattices obtained by adjusting the intensity and relative phase of the RF fields. In all cases: $d=0$, $z_0=2.0\ \mu$m, $S_{\rm dc}=2\ \mu$m, $S_{\rm RF}=2\ \mu$m, $B^E_{{\rm RF},y}=0.3$ G. Other parameters are: (a) $B^0_{\rm dc}=B^0_{\rm RF}=2$ G, $B^E_{{\rm RF},x}=0.19$ G; (b) $B^0_{\rm dc}=B^0_{\rm RF}=2$ G, $B^E_{{\rm RF},x}=0.49$ G; (c) $B^0_{\rm dc}=B^0_{\rm RF}=2$ G, $B^E_{{\rm RF},x}=0.19$ G, $\phi=\pi/8$, $\psi=\pi/3$; and (d) $B^0_{\rm dc}=B^0_{\rm RF}=1.7$ G, $B^E_{{\rm RF},x}=0.17$ G, $\phi=\pi/8$, $\psi=0$.

$$\boldsymbol{B}_{{\rm RF},\perp}=\left(B^E_{{\rm RF},x}\cos\theta\cos\psi-B_{{\rm RF},z}\sin\theta-B^E_{{\rm RF},y}\sin\phi\right)\hat{\boldsymbol{x}}'+\left(B^E_{{\rm RF},x}\cos\theta\sin\psi+B_{{\rm RF},y}+B^E_{{\rm RF},y}\cos\phi\right)\hat{\boldsymbol{y}}', \tag{8}$$

$$\boldsymbol{B}_{\rm dc}=\sqrt{B^2_{{\rm dc},x}+B^2_{{\rm dc},z}}\,\hat{\boldsymbol{z}}', \tag{9}$$

with a spatially varying $\tan\theta(x,\ z) = B_{\mathrm{dc},x}/B_{\mathrm{dc},z}$, and phases ϕ and ψ as defined in equation (6). The components of the fields are defined in the coordinate system in figure 1.

In figure 4, we give examples of lattices that can be defined from adjusting the intensity of fields as well as the relative phase between the applied RF fields. For simplicity, we consider the single filament limit to evaluate the fields intensities and neglect the vertical distance between conductor arrays ($d = 0$). The square lattice of double-well potentials shown in figure 4(c) results from setting an external field with elliptic polarization, $\phi = \pi/8$ and $\psi = \pi/3$. The array of two-leg ladders in figure 4(d) can be defined by setting $\phi = \pi/8$ and $\psi = 0$.

4. Experimental feasibility

Atom-chips are natural platforms for realizing the RF periodic potential proposed here. The micron-scale configuration of conductors in figure 2, as considered in the previous section 3, can be produced by standard micro-fabrication technology [10]. Here we briefly discuss some possibilities and obstacles for realizing and operating this device.

4.1. Landau–Zener losses

Kinetic coupling of atomic states produces atom-losses in radio-frequency dressed potentials. Such losses can be modelled as non-adiabatic Landau–Zener transitions along the direction of tightness confinement, which for atoms in the vibrational ground states of harmonic dressed trapping potential are approximately [31]

$$\Gamma_{\mathrm{LZ}} = \frac{2\omega_z}{\pi} \mathrm{e}^{-\pi V_{adb}(z_{\min})/(2\sqrt{2}\hbar\omega_z)}. \tag{10}$$

As a rule of thumb, small transition rates occur whenever the bottom of the dressed potential is much larger than the trapping frequency. In the configuration discussed here, such a condition can be meet by applying an external uniform RF field with sufficiently large amplitude. This is because a large uniform external field smooths out the spatial variation of the total field (and thus diminishes the trapping frequency) while simultaneously increases the minima of potential energy. In this case, the external RF-field plays a role similar to that of offset fields in static magnetic traps, which are needed to reduce Majorana spin-flips [10]. For the parameters used in figure 3, the relevant trapping frequency is $\omega_z/2\pi \approx 6$ kHz, while $V_{adb}(z_{\min})/2\pi\hbar \approx 100$ kHz, giving $\Gamma_{\mathrm{LZ}} \approx 10^{-3}$ Hz. In general terms, for micron-sized trapping configurations, the trap frequency is expected to be larger than 10^3 Hz, which requires, to produce a transition rate of 0.1 Hz, a field/current configuration such that $V_{adb}(z_{\min}) > 10\hbar\omega_z$. This will ensure that atoms experience the periodic potential for periods of time long enough to display complex many-body dynamics [2].

4.2. Microfabrication

Modern atom-chips include complex patterns of micron-sized structures made of a variety of materials, including metallic conductors [32], superconducting wires [33] and permanent magnets [16]. These structures can be defined with extremely high precision, such that edge defects and bulk features size are a few tens of nm [16, 32]. Also, micron-sized conductors can tolerate large current densities ($\sim 10^7$ A cm^{-2}), constrained mainly by the effectiveness of the setup to remove the heat generated by electric flow [28]. The potential landscape experienced by cold atoms in the vicinity of atom-chips can be tailored to a scale of 1–100 μm [10, 15], depending on the operational atom-surface distance and the size of the elements on the atom-chip.

Large arrays of current-carrying micron-sized parallel conductors have been already experimentally demonstrated. For example, in [34], Günther *et al* use an array of 372 parallel conductors of cross-section 1×0.3 μm, separated by gaps of 1 μm and carrying a current density of 7×10^4 A cm^{-2} which corresponds to a field $B^0_{\mathrm{dc}} = 0.21$ G. Theoretical and experimental work on atom-chips suggest that conductors of submicron dimensions can tolerate substantially larger current densities than used in [34]. For example, tests on a 700 nm wide 140 nm high conductor demonstrated a current density tolerance of 6×10^7 A cm^{-2} under dc operation for 10 s [28]. Such a current density produces a surface field of intensity $B^0_{\mathrm{dc}} = 84$ G, sufficiently large to create a strong trapping potential of a few tens of kHz holding the atoms a few microns away from its surface.

The condition of relative phase and current direction required for the RF-lattice can be enforced by the design of the conductor array. The array of Günter *et al* consists of a pair of meandering wires arranged such that neighbouring conductors carry currents in opposite directions, as required for our proposed device. In addition, various meandering paths can be combined which would give freedom for defining more complex periodic field distributions, including doubly periodic arrays (or superlattices), by applying different currents on each path.

Fabrication defects resulting in the undesired modification of a conductor's shape can have a substantial impact on the smoothness of *magnetic* traps produced with atom-chips (see, e.g. [35]). In contrast, in the present case, the spatial periodicity and dressed nature of the lattice ensures that such geometrical defects have little impact on the resulting dressed potential landscape. There are two key reasons for this. Firstly, the

inhomogeneities of the field associated with deformations of the conductor are exponentially suppressed with the distance from the conductor's surface [36]. The decay constant is of order π/Δ, with $\Delta \approx 1 - 10$ nm as the scale of the deviations of the conductor's edge from a straight line [14, 36]. Assuming that the conductors are all well defined, i.e. that $\pi/\Delta \gg \pi/S_{\mathrm{dc,RF}}$, the irregular field will have a negligible effect on the potential landscape at distances of the order $S_{\mathrm{dc,RF}}$. Secondly, RF-dressed potentials are significantly less sensitive to irregularities of the magnetic field distribution [37], offering additional protection from irregularities of the current flow.

Also relevant for the proposed device is the development of multilayer atom-chips with ultra-thin interlayer separation [38]. Experimental tests indicate that the thermal characteristics and current tolerance of micron-sized conductors of such devices have similar to those of single layer atom-chips [28, 38] .

4.3. Near-surface effects

The periodicity of the potential landscape is imposed by the dimensions of the conductor array, and is closely connected to the rapid decay of the field amplitude with distance from the surface. This requires us to set the lattice centre at close proximity of the chip surface. However, near surface effects impose constrictions on the operational parameters required to manipulate and keep the atoms a short distance from the surface [39–41]. Such effects are typically of two types. First, there is a strong atom-surface attractive interaction that deforms the trapping potential and, second, there is the interaction of the atomic magnetic moment with thermally produced low-frequency electromagnetic fields in the vicinity of the atom-chip conductors. Also, it is possible that the surface of the atom-chip would have a highly reflective layer as part of a mirror-MOT for loading purposes [28]. To estimate near-surface effects over the RF-dressed periodic lattice, we assume here that the surface in closest proximity to the atom is a 0.3 μm thick layer of gold.

Mutually induced dipole moments between trapped atoms and the atom-chip body create a strongly attractive van de Waals force, that can deform the trapping potential and lead to atoms being adhered to the device surface [39]. Such a force depends on the surface material and geometry and atomic level structure, and it is particularly intense at submicron atom-surface separations [39, 42]. The current and field configuration of the RF-lattice should produce a trapping potential strong enough to balance the attractive force. This requires a trapping frequency larger than a critical value that depends on the trap position and surface material [15]. For distances of the order of $z_{\min} \approx 1$ μm and in proximity to a reflecting layer, the trap frequency transverse to the atom-chip surface should satisfy $\omega/2\pi > \omega_{\mathrm{crit}}/2\pi \approx 0.32$ kHz. Our results show that the RF-lattice device, operating within the typical range of tolerable current densities, can create a trapping potential at a distance of $\sim$2 μm, with $\omega_z/2\pi \approx 6$ kHz (see figure 3(b)), which is capable of sufficiently compensating the surface attraction.

Johnson noise associated with the thermal current in the conductors induce atomic spin flips that result in losses from the trapping potential. Since at low frequencies the spectral density of the noisy field around micron-sized conductors is independent of the frequency [39], the loss rate of dressed atomic states is of the same order as in the case of spin-flip transitions in magnetic traps [10]. The thermal spin-flip rate corresponding to a conducting film of thickness $t \ll z_{\min}$ and resistivity ρ is given by [10]:

$$\Gamma_{\mathrm{Thermal}} \approx \left|\langle F,\, m+1|\, S_+ \,|F,\, m\rangle\right|^2 \left(\frac{3\mu_0 g_s \mu_B}{8\hbar}\right)^2 \frac{k_B T}{6\pi\rho}\frac{t}{z_{\min}^2}, \tag{11}$$

where the states $|F,\, m\rangle$ are defined with respect to the local quantization axis z in the rotating frame. For a gold reflecting film of thickness $t \approx 300$ nm at room temperature, and $z_{\min} \approx 2.0$ μm, the noise induced loss rate is approximately $\Gamma_{\mathrm{Thermal}} \approx 0.66$ Hz. This is dominant over non-adiabatic losses and determines a limit to the time scale of processes that can be studied with an RF-dressed lattice.

5. Bose–Hubbard parameters of a rectangular symmetric RF-lattice potential

At sufficiently low temperatures and densities, the dynamics of ultracold neutral atoms in a periodic potential is described by the Hubbard model, which is parametrized by inter-well tunnelling rates, J, and on-site the inter-particle interaction, U, defined in [1, 2, 17, 43]. In the Bosonic case, the Bose–Hubbard model presents superfluid and insulating phases determined by the ratio J/U. The transition between these two phases has been experimentally observed with ultracold atoms in 2D optical lattices, where J and U can be adjusted by changing the power and frequency of laser radiation defining the potential landscape [6].

Here we evaluate the possibility of observing the superfluid-insulating transition with atoms in the 2D dressed periodic potential presented before. For concreteness, we evaluate J and U corresponding to the parameters considered in figure 3. We employ a numerical routine for lattice Wannier states [43], which requires the Fourier components of the potential landscaped given by equation (5). In our trapping scheme,

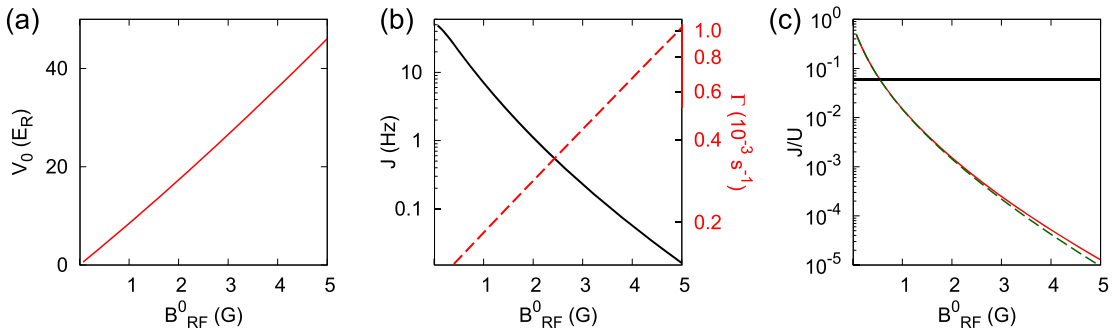

Figure 5. Bose–Hubbard parameters corresponding to the potential landscape for the state $|F = 1 m_F = -1\rangle$ of ^{87} Rb produced by a configuration with parameters as in figure 3: $w_{dc} = w_{RF} = 0.5$ μm, $S_{RF} = 1.0$ μm, $S_{dc} = 1.5$ μm, $z_0 = 2.0$ μm, $\omega_{RF} = 84.9$ kHz, $B^0_{dc} = 2.0$ G, and $B^E_{RF,y} = 0.3$ G. (a) Inter-well barrier (in units of the recoil energy $E_R = \hbar^2 k_{dc}^2/2m \approx h \times 254.82$ Hz) as a function of B^0_{RF}. (b) Tunnelling rate between neighbouring sites (solid) and atom-losses rate (dashed) (c) J/U ratio as function of B^0_{RF} for the RF dressed lattice (solid line) and a corresponding optical lattice (dashed line). The horizontal line indicates the critical value of the superfluid-to-Mott-insulator phase transition in a 2D Bose–Hubbard model [6].

both J and U are controlled by the amplitude of the total RF field (or, equivalently, the current in the RF conductors).

Figure 5(c) presents the ratio J/U as a function of the amplitude of the RF-field at the surface of the RF conductors (solid line), with other fields and currents adjusted to create a rectangular-symmetric periodic potential, as explained before. For comparison, we plot the Hubbard parameters corresponding to an optical lattice with matching period and amplitude (dashed line) defined by

$$V_{OL}(x, y) = V_0\Big(\sin^2\left(k_{dc}x\right) + \sin^2\left(k_{RF}y/2\right)\Big), \tag{12}$$

where V_0 is proportional to the intensity of the optical field and the wavelengths of the lattice fields are $\lambda_x = 2S_{dc}$ and $\lambda_y = 4S_{RF}$, along the x and y directions, respectively.

These results suggest that proven atom-chip technology will allow us to define RF-dressed lattice configurations with access to the parameters within the range demonstrated in optical lattices [6], including depth and periodicity. In particular, the ratio $J/U = 6.0 \times 10^{-2}$, critical for a superfluid-insulating transition in a symmetric 2D Bose–Hubbard model, is accessible with low-current densities that do not compromise the integrity of the device.

The experimental realization of the superfluid-Mott transtion requires a extremly low temperature of the atomic cloud. Roughly speaking, the thermal energy should be smaller than variations of the potential energy landscape, such that tunnelling and on-site interaction dominate over thermal motion. This condition is more difficult to satisfy for a large lattice period, because then a finite tunnelling needs low inter-well energy barriers. Since currently the lowest temperature achievable with cold atoms is in the range of 100 nK, the superfluid-Mott transition can only be observed with lattice periods of fraction of a micron, as in [6]. The analysis in section 4 and results in figure 5 suggest the feasibility of scaling down the RF-lattice to produce such lattice periods, utilizing sub-micron fabrication technique [21] and operating the lattice at close proximity of the chip, i.e. setting $z_0 \approx 1$ μm.

6. Summary and conclusion

In this work we have investigated possibilities for creating periodic potentials for ultracold atomic alkali atoms using the dressing of Zeeman split levels. The required spatially inhomogeneous dc and RF fields are produced by a pair of arrays of current carrying conductors and an uniform RF field. We demonstrate that standard atom-chip technology can be used to create RF-dressed periodic potentials with features in the range of a few microns, and therefore comparable with some applications of optical lattices (in particular [6]). The main restriction on an experimental realization of our proposed platform is from the limits of microfabrication technology and material properties.

In our proposed scheme, the features of the potential landscape are determined by the dimensions of the conductors. However, because of the fast decay of the field amplitude and the limitations on the maximum current that microfabricated conductors can tolerate, the RF frequency and field amplitudes should be set such that the trapping plane is formed at a distance comparable with the conductor's size. With currently proven technology for atom chips, the proposed device can easily produce potential landscapes with spatial periods in

the range between 1 and 10 μm, and therefore be suitable for applications of quantum information processing as suggested in [16, 29], simulation of Hubbard models and realization of lattice clocks. Importantly, the device we have presented here enables us to define lattice potentials with sub-micron periodicity by applying strong enough currents that either balance the surface attraction [39, 42], or allow us to define the trapping region far away from the atom-chip surface (i.e. larger than the separation and dimension of the conductors) where surface effects are weak.

Loading schemes used for other lattices (e.g. [16] and [29]) can be applied to the present situation without major difficulties. Nevertheless, to avoid splin-flips due to non-adiabatic effects during the loading procedure, it is important to keep a finite dressing at the plane of resonant driving. This can be done via the external applied RF field, which should be large enough to guarantee adiabatic conditions for the trap [23].

The lattice resulting from the simple array of conductors considered here can be easily varied from an array of 1D periodic potentials to a rectangular symmetric 2D lattice. Importantly, a significant advantage of our scheme over other proposals is the possibility of defining complex lattice potentials utilizing a very simple layout of conductors, simply by adjusting the relative phase between the applied RF fields. Examples of these cases are the lattice of double well potentials and the array of ladders shown in the text. It is straightforward to envisage more complex arrays of conductors and phase patterns to define lattices of interest for quantum simulation of quantum magnetism, including triangular and honeycomb geometries as well as superlattice potentials. Notice also that the design can be enriched by the addition of other dressing fields coupling states in different hyperfine manifolds of the ground state, e.g., the pair of states $|F=1,\ m_F=-1\rangle$ and $|F=2,\ m_F=1\rangle$ of ^{87}Rb, which are trapped in the transverse direction since they have a positive product $m_F g_F$. This will allow us to realize various applications including spin–orbit potentials [44], qubit encoding and entanglement generation for quantum information processing [45] as well as control over the sensitivity of atomic transitions for atomic clocks [46]. The close proximity of the lattice to the chip surface will allow single site addressing via the interaction with controllable microfabricated structures part of the atom-chip [22]. Important advantages of the present scheme over optical lattice realizations are the absence of spontaneous emission from the ground state manifold [47], as well as the strong mechanical and electric stability of atom-chips.

Acknowledgments

We gratefully acknowledge comments and input from Kathryn Burrows and Ross Williams. This work was supported by EPSRC grant EP/I010394/1.

Appendix A. Periodic dressed potential with an uniform RF field

Here we describe how the device in figure 1 produces a periodic potential landscape for cold atoms. A top view of the unit cell of the conductor array is shown in figure A1 (a), where we also indicate the coordinate system used for our analysis. For simplicity, we consider conductors in the limit of a single filament where the RF and dc fields have the harmonic spatial dependence given by equation (4), and there is an external uniform RF field with components $(B^E_{\mathrm{RF},x},\ B^E_{\mathrm{RF},y}>0,\ 0)$ (green arrow in figure A1(a)).

The dressed energy in equation (3) depends on two spatially varying contributions: first, the detuning of the RF frequency with respect to local Zeeman splitting, and second, the component of the RF field orthogonal to the local static field. To find a global minima of the potential energy it is convenient to analyse the potential landscape at surfaces of constant detuning, which correspond to planes parallel to chip surface parametrized by the distance z. It is also convenient to parametrize the y component of the external field by $B^E_{\mathrm{RF},y} = B^0_{\mathrm{RF}} e^{-k_{\mathrm{RF}}(z_E+d)}$. In this form, it is clear that at the plane z_E, the y component of the external RF field is compensated exactly by the field produced by the RF conductors at positions $(x,\ y,\ z)=(0,\ 2nS_{\mathrm{RF}},\ z_E)$, with $n\in\mathbb{Z}$. With this parametrization, the total dc and RF fields are given by

$$\boldsymbol{B}_{\mathrm{dc}} = B^0_{\mathrm{dc}} e^{-k_{\mathrm{dc}}z}(\cos(k_{\mathrm{dc}}x),\ 0,\ -\sin(k_{\mathrm{dc}}x)), \tag{A.1}$$

$$\boldsymbol{B}_{\mathrm{RF}} = B^0_{\mathrm{RF}} e^{-k_{\mathrm{RF}}(z+d)}\Big(B^E_{RF,x},\ -\cos(k_{\mathrm{RF}}y) + e^{-k_{\mathrm{RF}}(z_E-z)},\ \sin(k_{\mathrm{RF}}y)\Big), \tag{A.2}$$

from which the component of the RF field orthogonal to the static field (defined as the effective dressing field) becomes

$$B^2_{\mathrm{RF},\perp} = \Big(B^0_{\mathrm{RF}} e^{-k_{\mathrm{RF}}(z_E+d)} - B^0_{\mathrm{RF}}\cos(k_{\mathrm{RF}}y)\, e^{-k_{\mathrm{RF}}(z+d)}\Big)^2 + \Big(B^0_{\mathrm{RF}}\cos(k_{\mathrm{dc}}x)\sin(k_{\mathrm{RF}}y)\, e^{-k_{\mathrm{RF}}(z+d)} + B^E_{\mathrm{RF},x}\sin(k_{\mathrm{dc}}x)\Big)^2. \tag{A.3}$$

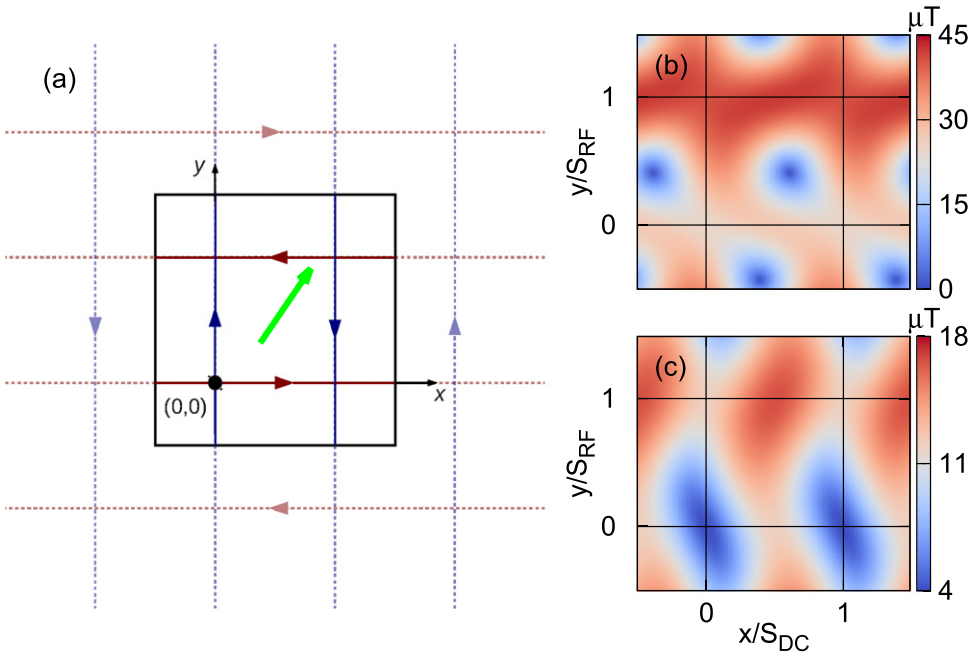

Figure A1. (a) Upper view of the conductor array in figure 2. The unit cell of the array is enclosed by a solid-line square. The origin of coordinates is highlighted by a black circle and the label (0, 0). Solid lines represent current carrying conductors. Other panels: Magnitude of the effective dressing field at (b) a plane below z_E and (c) the resonant plane z_0. The colour bar corresponds to the parameters:: $w = 0$, $S_{\rm dc} = 2.0\ \mu$m, $S_{\rm RF} = 1.5\mu$m, $z_0 = 2.0\ \mu$m, $B^0_{\rm RF} = 6.2$ G, $B^0_{\rm dc} = 2.0$ G, $\omega_{\rm RF} = 3.8 \times 10^5$ rad s^{-1}, $B^E_{{\rm RF},x} = 114.3$ mG, and $B^E_{{\rm RF},y} = 80.1$ mG. In (b) the field is evaluated at $z = 1.0\ \mu$m.

As shown in figure A1(b), at planes between the chip surface and z_E (i.e. $z < z_E$) there are positions where $B_{{\rm RF},\perp} = 0$. These locations occur along the lines parallel to the y axis where $B^E_{{\rm RF},y}$ is compensated by the conductor's field. These are defined by the relation $\cos(k_{RFy}) = {\rm e}^{-k_{\rm RF}(z_E - z)}$. Along these lines, the dressing field is restricted to the x–z plane. Noticing that the static field also lie in the x–z plane and that its direction varies continuously between $-\pi$ and π along the unit cell, we conclude that there are positions where the RF and dc fields are either parallel or anti-parallel, making $B_{{\rm RF},\perp} = 0$. This situation can be seen in figure A1(b), where the effective dressing field becomes zero at various locations within the unit cell, marked as dark spots. Thus, the dressed energy at planes $z < z_E$ have a minimal value equal to the detuning $V_{\rm min}\ (z < z_E)$ $= \mu_B g_F B^0_{\rm dc}({\rm e}^{-k_{\rm dc} z} - {\rm e}^{-k_{\rm dc} z_0})$. Another consequence is that setting the external field such that $z_E < z_0$ avoids a zero effective dressing field at the resonant plane. Also, since the detuning increases monotonically with the distance from the resonant plane z_0, we conclude that a global minimum of the dressed energy should be located above z_E.

It can be easily verified algebraically and numerically that at planes above z_E, the effective dressing field has four critical points: one local minimum at $(0,\ 0)$, two saddle points at $(0,\ S_{\rm RF})$ and $(0.5S_{\rm dc},\ 0)$, and a local maxima at $(0.5S_{\rm dc},\ S_{\rm RF})$, as shown in figure A1(c). This implies that a global minimum of the dressed energy should be located along the z axis, between locations of minimal effective dressing, z_E, and minimal detuning, z_0. More precisely, since the the potential energy along the line $(0,\ 0,\ z)$ is given by

$$V(0,\ 0,\ z) = \sqrt{\left(B^0_{\rm dc}\left({\rm e}^{-k_{\rm dc} z} - {\rm e}^{-k_{\rm dc} z_0}\right)\right)^2 + \frac{1}{4}\left(B^0_{\rm RF}{\rm e}^{-k_{\rm RF} d}\left({\rm e}^{-k_{\rm RF} z} - {\rm e}^{-k_{\rm RF} z_E}\right)\right)^2}, \tag{A.4}$$

the minimum occurs at the position where the condition

$$\left(B^0_{\rm RF}\right)^2 k_{\rm RF}{\rm e}^{k_{\rm RF}(z+d)}\left({\rm e}^{k_{\rm RF} z} - {\rm e}^{k_{\rm RF} z_E}\right) = 4\left(B^0_{\rm dc}\right)^2 k_{\rm dc}{\rm e}^{k_{\rm dc} z}\left({\rm e}^{k_{\rm dc} z} - {\rm e}^{k_{\rm dc} z_0}\right) \tag{A.5}$$

is satisfied.

Equation (A.5) does not have an analytic solution for a general set of parameters. Nevertheless, it is instructive to find a solution for a simplified situation where $k_{\rm dc} = k_{\rm RF} = k, d = 0$ and $B_{\rm dc} = B_{\rm RF}$. In this case, the dressed potential energy has a minimum at

$$z_{\rm min} = z_0 - \frac{1}{k}\left(\ln\left(4 + {\rm e}^{-k(z_E - z_0)}\right) - \ln(5)\right). \tag{A.6}$$

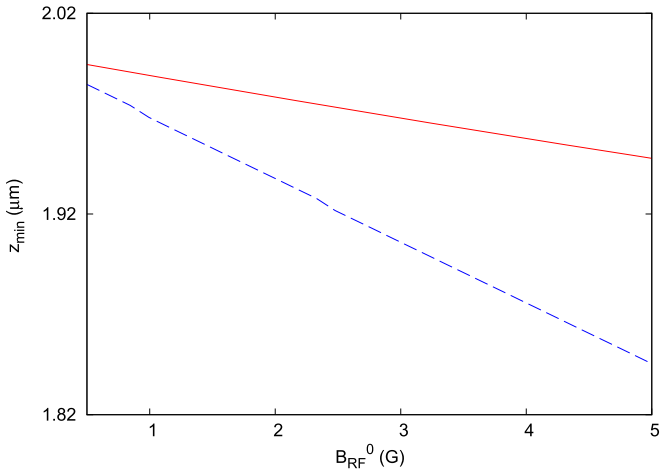

Figure A2. Numerical evaluation of the trap position, as function of the RF maximal field, for a rectangular symmetric lattice configuration. Solid line: conductors of finite size $w_{dc} = w_{RF} = 0.5$ μm. Dashed line: solution of equation (A.5) corresponding to the single filament model, $w_{dc} = w_{RF} = 0.0$. Other parameters $d = 400$ nm, $S_{RF} = 1.0$ μm $S_{dc} = 1.5$ μm, $z_0 = 2.0$ μm, $B_{dc}^0 = 2.0$ G, and $B_{RF,y}^E = 0.3$ G.

This equation allows us to estimate the vertical position of the RF lattice for the parameters used in figure 3, setting $k = k_{dc}$. However, we notice that in this particular case, the conductor's finite size ensures that the distance between the lattice and the resonant plane is significantly smaller than the value given by equation (A.6). This is shown in figure A2 where we plot z_{min} evaluated numerically (solid line) and given by equation (A.6) with $k = k_{dc}$. This difference occurs because in close proximity of finite size conductors (i.e. $w > 0$ and $z_0 \approx w$) the amplitude of the fields decay much slower than an exponential damping.

Appendix B. Field produced by an array of finite conductors

The magnetic field produced by a current carrying conductor depends on its geometry at distances comparable with the conductor dimensions. The present application requires us to calculate the magnetic field produced by an array of conductors of finite with and negligible height, where the current direction alternates between neighbouring wires (as in figure 1(b)). Such a field can be calculated using:

$$B_{dc,x} = 2B_{dc}^0 \sum_{i=-N/2}^{N/2} (-1)^{i-1}\left(\arctan\left(\frac{x - x_i - w_{dc}/2}{z}\right) - \arctan\left(\frac{x - x_i + w_{dc}/2}{z}\right)\right), \tag{B.1}$$

$$B_{dc,y} = 0, \tag{B.2}$$

$$B_{dc,z} = -B_{dc}^0 \sum_{i=-N/2}^{N/2} (-1)^{i-1} \ln\left(\frac{(x - x_i - w_{dc}/2)^2 + z^2}{(x - x_i + w_{dc}/2)^2 + z^2}\right), \tag{B.3}$$

with $N + 1$ as the total number of conductors and $x_i = -\frac{1}{2}(N + 1)S_{dc} + (i - 1)S_{dc}$ being the centre of the ith dc conductor (in the numerical work we use $N = 500$). Similarly, the field produced by the orthogonal array carrying RF currents can be evaluated using equations (B.1)–(B.3) after the substitutions dc → RF, $x \to y$, $x_i \to y_i$, $z \to z + d$ and $B_x \to B_y, B_x = 0$.

References

[1] Lewenstein M *et al* 2007 Ultracold atomic gases in optical lattices: mimicking condensed matter physics and beyond *Adv. Phys.* **56** 243–379
[2] Bloch I, Dalibard J and Zwerger W 2008 Many-body physics with ultracold gases *Rev. Mod. Phys.* **80** 885–964
[3] Polkovnikov A, Sengupta K, Silva A and Vengalattore M 2011 Colloquium *Rev. Mod. Phys.* **83** 863–83
[4] Banerjee D *et al* 2013 Atomic quantum simulation of **U**(*n*) and SU(*n*) non-abelian lattice gauge theories *Phys. Rev. Lett.* **110** 125303
[5] Bloch I 2005 Ultracold quantum gases in optical lattices *Nat. Phys.* **1** 23–30
[6] Spielman I B, Phillips W D and Porto J V 2007 Mott-insulator transition in a two-dimensional atomic Bose gas *Phys. Rev. Lett.* **98** 080404

[7] Struck J *et al* 2011 Quantum simulation of frustrated classical magnetism in triangular optical lattices *Science* **333** 996–9
[8] Jotzu G, Messer M, Desbuquois R, Lebrat M, Uehlinger T, Greif D and Esslinger T 2014 Experimental realization of the topological Haldane model with ultracold fermions *Nature* **515** 237–40
[9] Lee P A, Nagaosa N and Wen X-G 2006 Doping a Mott insulator: physics of high-temperature superconductivity *Rev. Mod. Phys.* **78** 17–85
[10] Fortágh J and Zimmermann C 2007 Magnetic microtraps for ultracold atoms *Rev. Mod. Phys.* **79** 235–89
[11] Gerritsma R *et al* 2007 Lattice of microtraps for ultracold atoms based on patterned magnetic films *Phys. Rev.* A **76** 033408
[12] Singh M *et al* 2008 One-dimensional lattice of permanent magnetic microtraps for ultracold atoms on an atom chip *J. Phys. B: At. Mol. Opt. Phys.* **41** 065301
[13] Ghanbari S, Kieu T D, Sidorov A and Hannaford P 2006 Permanent magnetic lattices for ultracold atoms and quantum degenerate gases *J. Phys. B: At. Mol. Opt. Phys.* **39** 847
[14] Schmied R, Leibfried D, Spreeuw R J and Whitlock S 2010 Optimized magnetic lattices for ultracold atomic ensembles *New J. Phys.* **12** 103029
[15] Leung V, Tauschinsky A, van Druten N and Spreeuw R 2011 Microtrap arrays on magnetic film atom chips for quantum information science *Quantum Inf. Process.* **10** 955–74
[16] Leung V *et al* 2014 Magnetic-film atom chip with 10 μm period lattices of microtraps for quantum information science with Rydberg atoms *Rev. Sci. Instrum.* **85** 053102
[17] Ghanbari S, Blakie P B, Hannaford P and Kieu T D 2009 Superfluid to Mott insulator quantum phase transition in a 2D permanent magnetic lattice *Eur. Phys. J.* **70** 305
[18] Grabowski A and Pfau T 2003 A lattice of magneto-optical and magnetic traps for cold atoms *Eur. Phys. J. D: At. Mol. Opt. Plasma Phys.* **22** 347–54
[19] Yun M and Yin J 2006 Practical scheme to realize 2d array of BECs on an atom chip: novel 2d magneto-optical and magnetic lattices *Opt. Express* **14** 2539–51
[20] Pollock S, Cotter J P, Laliotis A, Ramirez-Martinez F and Hinds E A 2011 Characteristics of integrated magneto-optical traps for atom chips *New J. Phys.* **13** 043029
[21] Herrera I *et al* 2015 Sub-micron period lattice structures of magnetic microtraps for ultracold atoms on an atom chip *J. Phys. D: Appl. Phys.* **48** 115002
[22] Romero-Isart O, Navau C, Sanchez A, Zoller P and Cirac J 2013 Superconducting vortex lattices for ultracold atoms *Phys. Rev. Lett.* **111** 145304
[23] Zobay O and Garraway B M 2001 Two-dimensional atom trapping in field-induced adiabatic potentials *Phys. Rev. Lett.* **86** 1195
[24] Lesanovsky I, Hofferberth S, Schmiedmayer J and Schmelcher P 2006 Manipulation of ultracold atoms in dressed adiabatic radio-frequency potentials *Phys. Rev.* A **74** 033619
[25] Garraway B M and Perrin H 2010 An effective scalar magnetic interaction for resonantly trapped atoms *Phys. Scr.* **2010** 014006
[26] Fernholz T, Gerritsma R, Krüger P and Spreeuw R J C 2007 Dynamically controlled toroidal and ring-shaped magnetic traps *Phys. Rev.* A **75** 063406
[27] Schumm T *et al* 2005 Matter-wave interferometry in a double well on an atom chip *Nat. Phys.* **1** 57–62
[28] Reichel J and Vuletic V 2010 *Atom Chips* (New York: Wiley)
[29] Jose S *et al* 2014 Periodic array of Bose–Einstein condensates in a magnetic lattice *Phys. Rev.* A **89** 051602
[30] Bermudez A, Patanè D, Amico L and Martin-Delgado M 2009 Topology-induced anomalous defect production by crossing a quantum critical point *Phys. Rev. Lett.* **102** 135702
[31] Morizot O, Colombe Y, Lorent V, Perrin H and Garraway B M 2006 Ring trap for ultracold atoms *Phys. Rev.* A **74** 023617
[32] Groth S *et al* 2004 Atom chips: fabrication and thermal properties *Appl. Phys. Lett.* **85** 2980–2
[33] Cano D *et al* 2008 Meissner effect in superconducting microtraps *Phys. Rev. Lett.* **101** 183006
[34] Günther A *et al* 2005 Diffraction of a Bose–Einstein condensate from a magnetic lattice on a microchip *Phys. Rev. Lett.* **95** 170405
[35] Krüger P *et al* 2007 Potential roughness near lithographically fabricated atom chips *Phys. Rev.* A **76** 063621
[36] Wang D-W, Lukin M D and Demler E 2004 Disordered Bose–Einstein condensates in quasi-one-dimensional magnetic microtraps *Phys. Rev. Lett.* **92** 076802
[37] van Es J J P, Whitlock S, Fernholz T, van Amerongen A H and van Druten N J 2008 Longitudinal character of atom-chip-based RF-dressed potentials *Phys. Rev.* A **77** 063623
[38] Trinker M *et al* 2008 Multilayer atom chips for versatile atom micromanipulation *Appl. Phys. Lett.* **92** 254102
[39] Lin Y-j, Teper I, Chin C and Vuletić V 2004 Impact of the Casimir–Polder potential and Johnson noise on Bose–Einstein condensate stability near surfaces *Phys. Rev. Lett.* **92** 050404
[40] Nirrengarten T *et al* 2006 Realization of a superconducting atom chip *Phys. Rev. Lett.* **97** 200405
[41] Sinuco-León G, Kaczmarek B, Krüger P and Fromhold T M 2011 Atom chips with two-dimensional electron gases: theory of near-surface trapping and ultracold-atom microscopy of quantum electronic systems *Phys. Rev.* A **83** 021401
[42] Judd T E, Scott R G, Martin A M, Kaczmarek B and Fromhold T M 2011 Quantum reflection of ultracold atoms from thin films, graphene and semiconductor heterostructures *New J. Phys.* **13** 083020
[43] Walters R, Cotugno G, Johnson T H, Clark S R and Jaksch D 2013 Ab initio derivation of Hubbard models for cold atoms in optical lattices *Phys. Rev.* A **87** 043613
[44] Kennedy C J, Siviloglou G A, Miyake H, Burton W C and Ketterle W 2013 Spin–orbit coupling and quantum spin Hall effect for neutral atoms without spin flips *Phys. Rev. Lett.* **111** 225301
[45] Yi W, Daley A J, Pupillo G and Zoller P 2008 State-dependent, addressable subwavelength lattices with cold atoms *New J. Phys.* **10** 073015
[46] Sárkány L, Weiss P, Hattermann H and Fortágh J 2014 Controlling the magnetic field sensitivity of atomic clock states by microwave dressing *Phys. Rev.* A **90** 053416
[47] Goldman N *et al* 2010 Realistic time-reversal invariant topological insulators with neutral atoms *Phys. Rev. Lett.* **105** 255302